Universität Hamburg
DER FORSCHUNG | DER LEHRE | DER BILDUNG

BACHELORTHESIS

The effect of the Milky Way magnetic field on photon-axion conversions

vorgelegt von

Friedrich Landgraf

03. September 2024

Fakultät für Mathematik, Informatik und Naturwissenschaften

Fachbereich Physik

Institut für Experimentalphysik

Studiengang: Physik, B.Sc (6. Semester)

Matrikelnummer: 7495815

friedrich.landgraf@studium.uni-hamburg.de

Erstgutachter: Prof. Dr. Dieter Horns

Zweitgutachter: Prof. Dr. Manuel Meyer

Abstract

The axion and axion like particles (ALPs) are among the most promising candidates for dark matter at the moment. One way to detect them is through their interaction with photons in the presence of a magnetic field. The python package gammaALPs calculates the oscillation probability between photons and ALPs in different astrophysical magnetic field environments, in order to compare the calculated photon survival rates with the measured γ-ray spectra of extragalactic sources in the search for ALPs. An important environment for the photon-ALP mixing is the galactic magnetic field (GMF) of the Milky Way. In this bachelor thesis a new model (consisting of eight versions) for the GMF of the Milky Way by Michael Unger and Glennys R. Farrar is implemented in gammaALPs. The thesis reviews the properties of the new model and the data that was used for fitting. It then gives an introduction to gammaALPs and shows how to use the newly implemented GMF model. The new model is then used to create full sky maps of axion-photon conversion probabilities and the results of the calculations are compared with the already implemented "jansson12" and "pshirkov" model at an example of two extragalactic γ-ray sources, NGC 1275 and GRB 221009A. The comparison shows that the calculated conversion probability can differ by up to a factor of 30 between the old and new models. However, the new model also includes versions with more similar results to the old models. This variety of new models, now implemented in gammaALPs, provides many opportunities for future analysis of photon-ALP mixing.

Zusammenfassung

Das Axion und axion-ähnliche Teilchen (ALPs) sind derzeit einer der vielversprechendsten Kandidaten für dunkle Materie. Eine Möglichkeit, sie nachzuweisen, ist ihre Wechselwirkung mit Photonen in Gegenwart von Magnetfeldern. Das Python-Paket gammaALPs berechnet die Oszillationswahrscheinlichkeiten zwischen Photonen und ALPs in verschiedenen astrophysikalischen Magnetfeldumgebungen, um die berechneten Photonenüberlebensraten mit gemessenen γ-Strahlenspektren von extragalaktischen Quellen zu vergleichen. Eine wichtige Umgebung für die Oszillation zwischen Photonen und ALPs ist das galaktische Magnetfeld (GMF) der Milchstraße. In dieser Bachelorarbeit wird ein neues Modell (bestehend aus acht Versionen) für das GMF der Milchstraße von Michael Unger und Glennys R. Farrar in gammaALPs implementiert. Die Arbeit gibt einen Überblick über die Eigenschaften des neuen Modells und die Daten, die für die Erstellung verwendet wurden. Anschließend wird eine Einführung in gammaALPs gegeben und es wird gezeigt, wie das neu implementierte GMF-Modell verwendet werden kann. Das neue Modell wird dann verwendet, um vollständige Himmelskarten der Axion-Photonen-Umwandlungswahrscheinlichkeiten zu erstellen, und die Ergebnisse der Berechnungen werden mit dem bereits implementierten „jansson12"- und „pshirkov"-Modell am Beispiel von zwei extragalaktischen γ-Strahlenquellen, NGC 1275 und GRB 221009A, verglichen. Der Vergleich zeigt, dass sich die berechnete Umwandlungswahrscheinlichkeit zwischen dem alten und dem neuen Modell um bis zu einem Faktor 30 unterscheiden kann. Das neue Modell enthält jedoch auch Versionen, deren Ergebnisse denen der alten Modelle ähnlicher sind. Diese Vielfalt an neuen Modellen, die nun in gammaALPs implementiert sind, bietet die Möglichkeit für verschiedene zukünftige Analysen der Photon-ALP-Oszillation.

Contents

List of Figures

List of Tables

Listings

1 Introduction

The nature of dark matter is one of the biggest unsolved problems in modern physics. Dark matter is hypothetical matter that does not interact with electromagnetic radiation, but can be observed through its gravitational effects on visible matter [1]. Today it is believed that dark matter makes up about 26 % of the universe's energy density, five times more than "normal" matter does [2].

An explanation for dark matter might be the axion, a particle that was introduced in the 1970s to solve the strong CP-problem (Section 2.2) and is now also considered a possible dark matter candidate.

One of the ways to detect axions or axion like particles (ALPs) is through their interaction with photons in the presence of a magnetic field. Magnetic fields close to a γ-ray source can convert photons into ALPs, which can then propagate undisturbed over large distances and convert back into photons in the magnetic field of the Milky Way. That could lead to features in the γ-ray spectra of extragalactic sources that could be measured and provide clues about axions [3].

The focus of this thesis will be on a new model for the magnetic field of the Milky Way by Michael Unger and Glennys R. Farrar [4]. The new model consists of eight models that are fit to the latest Faraday rotation measures and polarized synchrotron intensity maps and it will be implemented into the python package gammaALPs, to be used for calculations of photon-ALP mixing. When implemented into gammaALPs, the new model can help analyse γ-ray spectra in the search for axion dark matter.

In the following sections I will first give a brief overview of dark matter, talk about evidence for dark matter and possible candidates (Section 2.1). Then I will go into more detail about the axion and ALPs, and the mechanism of photon-ALP mixing (Section 2.2 and Section 2.3). After that I will discuss the data that is used to model galactic magnetic fields (Section 3.1) and give a few examples for already existing models before going into more detail about the new Unger-Farrar model in Section 4. In the final section I will describe the python package gammaALPs (Section 5.1) and discuss the implementation of the new magnetic field model (Section 5.2). Then I will show the applications of the new model in gammaALPs by creating full sky maps for photon-axion conversion probabilities (Section 5.3). In the end I will compare the results of the new models to the two already implemented models using two examples of extragalactic γ-ray sources, NGC 1275 and GRB 221009A (Section 5.4).

2 Theoretical background

2.1 Dark Matter

The standard model and its limits

The standard model (SM) of particle physics is one of the most successful theories of modern science. Its big achievement is the unified description of three of the four fundamental forces (strong, weak and electromagnetic force, excluding gravity) [5].

The SM consists of 17 elementary particles (see Fig. 1) that can be divided into three groups [6]. There are twelve particles with spin 1/2 called fermions which make up matter. They can be grouped into six flavors of quarks, three flavors of charged leptons and three flavors of neutral leptons. Additionally, each fermion has a corresponding antiparticle with same mass but opposite charge.

Beside the matter particles there are four gauge bosons with spin 1. They are known as the force carrying particles with the photon γ for the electromagnetic force, the gluons g for the strong force and the $W^{\pm}$ and Z bosons for the weak interactions.

The 17th particle is the Higgs-Boson. It is a scalar boson with spin 0. The mechanism concerning the Higgs-Boson gives mass to the massive elementary particles and it was only discovered in 2012 at the Large Hadron Collider [7].
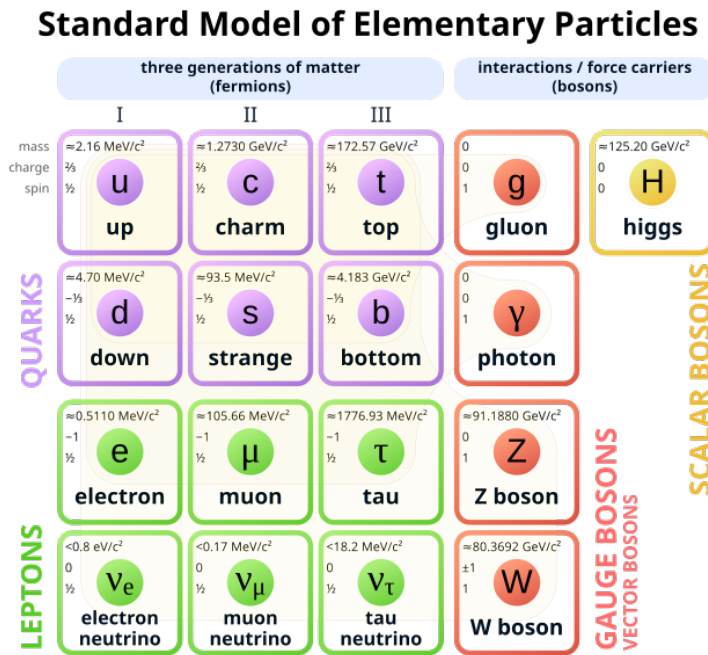
Figure 1: The 17 elementary particles of the standard model with mass, charge and spin [8].

Despite its success, the standard model is not a complete theory. It fails to include gravity, the weakest of the fundamental forces. Gravity is described by the general theory of relativity, but even in partnership with general relativity the standard model does not account for several astronomical observations, that could be explained with "Dark Matter", for which the SM does

not contain a clear candidate [9].

Evidence for dark matter

Although no dark matter particle has yet been found, there is clear evidence that dark matter exists. One of the most convincing evidence for dark matter comes from the study of galactic rotation curves [1]. In galaxies all stars and matter orbit around the center due to gravity. According to newtonian mechanics the velocity should be falling $\propto 1/\sqrt{r}$ beyond the optical disc [10]. However, observations in the 1970s like those of Rubin and Ford (for an example see [11]) show an almost flat rotation curve for outer regions of galaxies. Similar observations of flat rotation curves have now been found for all galaxies studied [1]. These observations imply, that galaxies contain far more mass than can be explained by visible matter.

Other evidence for dark matter is provided by the gravitational lensing effect. According to Einstein's theory of general relativity, massive objects can bend the path of light and act like a lens. Using this effect, astronomers can map the distribution of mass in the lensing object. Observations have shown that a lot of the matter necessary to create the observed lensing effects have to be dark matter (see for example [12], [13]).

The information to estimate the total amount of dark matter in the universe can be extracted from the analysis of the Cosmic Microwave Background (CMB) [10]. The CMB is microwave radiation (~ 160 GHz) from the hot early days of the universe that fills all the space in the observable universe. The CMB is isotropic at the 10^{-5} level and the analysis of its anisotropies reveals information about the energy densities of the universe [10]. Today's results show, that normal matter (baryonic matter) makes up only about 5 % of the total energy density, while dark matter is about five times more prevalent with about 26 %. The other 69 % are an unknown form of energy called dark energy [2].

Candidates for dark matter

Twenty-five years ago one possible candidate for dark matter were massive compact halo objects (MACHOs). MACHOs include stellar objects of baryonic matter to faint to be discovered. However, research has shown that they can't account for all dark matter and that nonbaryonic candidates beyond the standard model are more likely [1].

One of the nonbaryonic candidates are the weakly interacting massive particles (WIMPs). They only interact with the gauge bosons of the weak force and have a mass in the range GeV - 10 TeV. WIMPs are predicted by many particle physics theories and naturally have the right relic density, but despite extensive searches have not yet been observed [1].

Another candidate that already exists in particle physics is the axion and it will be the focus of the following work.

2.2 Fundamentals of axions and ALPs

Axions and axion like particles (ALPs) are hypothetical particles that arise in many different particle physics theories. The axion is motivated by the strong CP problem in quantum chromodynamics (QCD) [6]. CP stands for charge conjugation symmetry (C) and parity symmetry (P). The SM Lagrangian contains a term that contributes to CP-violation, like an electric dipole moment (EDM) of the neutron. However, experimental measurements already imply an either extremely small or zero EDM of the neutron, which makes this a fine-tuning problem [6].
One solution was proposed by Peccei and Quinn in 1977 [14]. They introduced a symmetry (PQ-Symmetry), which, when broken, would lead to a new pseudoscalar boson, which was identified as the axion by Weinberg [15] and Wilczek [16]. The axion mass is determined by the scale f_a (axion decay constant) at which the PQ-symmetry is broken and given by: [6]

$$m_a = \frac{\sqrt{m_u m_d}}{m_u + m_d} m_\pi f_\pi \frac{1}{f_a} \approx 6\,\mu\text{eV} \left(\frac{10^{12}\,\text{GeV}}{f_a} \right) \tag{1}$$

where m_u, m_d and m_π are the masses of the up-quarm, down-quark and pion, and f_π is the pion decay constant. The very high axion decay constant of $f_a \geq 4 \cdot 10^8$ GeV leads to a small axion mass $m_a \leq 15$ meV [17].

The phenomenology of ALPs is qualitatively the same, but they do not solve the strong CP-problem [18]. That removes the connection between the mass m_a and decay constant f_a, making ALPs a more general case of the axion.

2.3 Photon-ALP mixing

Photon-ALP mixing is an important theoretical mechanism that allows for the conversion between photons and axions/ALPs. This mechanism is fundamental to the search for ALPs.
Below is a summary of the equations of motion for photon-ALP mixing, and formulas to calculate conversion probabilities, closely following [3] and [19].
The effective Lagrangian for the mixing can be written as

$$\mathscr{L} = \mathscr{L}_{a\gamma} + \mathscr{L}_{EH} + \mathscr{L}_a \tag{2}$$

where $\mathscr{L}_{a\gamma}$ is the Lagrangian for the coupling of ALPs to photons, $\mathscr{L}_{EH}$ is the effective Euler-Heisenberg Lagrangian and $\mathscr{L}_a$ contains the ALPs mass and kinetic terms [3]. The coupling of ALPs to photons is described by

$$\mathscr{L}_{a\gamma} = -\frac{1}{4} g_{a\gamma} F_{\mu\nu} \tilde{F}^{\mu\nu} a \tag{3}$$

where a is the ALP field strength, $g_{a\gamma}$ is the coupling constant, and $F_{\mu\nu}$ and $\tilde{F}^{\mu\nu}$ is the electromagnetic field tensor and its dual. So it can be also written as:

$$\mathscr{L}_{a\gamma} = -\frac{1}{4}g_{a\gamma}a\boldsymbol{E}\boldsymbol{B} \tag{4}$$

with the electric field $\boldsymbol{E}$ and magnetic field $\boldsymbol{B}$ [18].
$\mathscr{L}_a$ is given by

$$\mathscr{L}_a = \frac{1}{2}\partial_\mu a\partial^\mu a - \frac{1}{2}m_a^2 a^2 \tag{5}$$

with the ALP mass m_a.

ALPs and photons only couple in a magnetic field that has a component that is transversal to the propagation direction. Let us assume the propagation direction is along the x_3 axis and the transversal magnetic field component is along the x_2 axis $\boldsymbol{B}_\perp = B\hat{\mathbf{e}}_2$. Then the ALPs only couple to photon polarisation states in the $x_2 - x_3$ plane. The equations of motion for a polarized photon beam of energy E in a cold plasma with a homogeneous magnetic field are given by:

$$\left(i\frac{\mathrm{d}}{\mathrm{d}x_3} + E + \mathscr{M}_0\right)\Psi(x_3) = 0 \tag{6}$$

with $\Psi(x_3) = (A_1(x_3), A_2(x_3), a(x_3))$, where A_1 and A_2 are the photon polarisation states along x_1 and x_2, respectively, and a the polarization state of the axion. $\mathscr{M}_0$ is the mixing matrix and it is given by:

$$\mathscr{M}_0 = \begin{pmatrix} \Delta_\perp & 0 & 0 \\ 0 & \Delta_\parallel & \Delta_{a\gamma} \\ 0 & \Delta_{a\gamma} & \Delta_a \end{pmatrix} \tag{7}$$

The terms $\Delta_{\perp,\parallel}$ arise due to effects of the propagation of photons in a plasma and the QED vacuum polarisation effect [3]. The kinetic term for the ALP is $\Delta_a = -m_a^2/(2E)$ and the terms $\Delta_{a\gamma} = g_{a\gamma}B/2$ lead to photon-ALP mixing.

For an unpolarised photon beam Equation (6) needs to be reformulated in terms of the density matrix $\rho(x_3) = \Psi(x_3)\Psi(x_3)^\dagger$ that obeys the von-Neumann-like commutator equation:

$$i\frac{\mathrm{d}\rho}{\mathrm{d}x_3} = [\rho, \mathscr{M}_0]. \tag{8}$$

Equation (6) is solved with $\Psi(x_3) = \mathscr{T}(x_3, 0; E)\Psi(0)$ and initial condition $\mathscr{T}(0, 0; E) = 1$, where $\mathscr{T}$ is called the transfer matrix and Equation (8) is solved through:

$$\rho(x_3) = \mathscr{T}(x_3, 0; E)\rho(0)\mathscr{T}^\dagger(x_3, 0; E). \tag{9}$$

The photon-ALP beam can travel through many different magnetic field environments between the source and the observer. For each environment $m = 1, ..., M$ the path can be split into N_m consecutive domains, so that the transfer matrix of each is found through matrix multiplication

and the final transfer matrix for all environments is given by: [19]

$$\mathscr{T}_{\text{tot}} = \prod_{m=1}^{M} \prod_{n=1}^{N_m} \mathscr{T}_{M-m+1}\left(x_{3,N_{M-m+1}-n+1}, x_{3,N_{M-m+1}-m}; E\right) \tag{10}$$

$m = 1$ is the environment closest to the source and $x_{3,0} = 0$ is the coordinate closest to the source. The total photon survival probability is then given by:

$$P_{\gamma\gamma} = \text{Tr}\left((\rho_{11} + \rho_{22})\mathscr{T}_{\text{tot}}\rho(0)\mathscr{T}_{\text{tot}}^{\dagger}\right) \tag{11}$$

with $\rho_{11} = \text{diag}(1,0,0)$, $\rho_{22} = \text{diag}(0,1,0)$, and the initial polarization $\rho(0)$ [19].

3 Modelling Galactic Magnetic Fields

Galactic magnetic fields (GMFs) are an important element of galaxies and have a big effect on many astrophysical processes. The GMF plays a crucial role in disk dynamics, cosmic-ray propagation, the turbulent interstellar medium and star formation [20]. Moreover, like all magnetic fields it has an effect on photon-ALP mixing, so a profound understanding of the GMF could help in detecting axions.

3.1 Data for modelling GMF

The modelling of the milky way GMF is based on various observables, like polarized starlight, Faraday rotation measures (RMs), diffuse polarized synchrotron emission, diffuse polarized thermal dust emission and diffuse γ-ray emission.
Additionally to the observables you need to make assumptions about the distribution of particles, like thermal electrons, relativistic cosmic rays or dust grains [20]. The different observables can then be used with the auxiliary models to model different properties of the GMF.

Polarized starlight
The galactic magnetic field can influence the starlight. When light passes through a region with amorphous dust particle, it can be polarized. Under the effect of the GMF the dust particles align their long axes perpendicular to the magnetic field, so the starlight is linearly polarized parallel to that local magnetic field as projected onto the sky from the observer's point of view [20]. In addition to the observable, one needs to know the dust distribution to analyse the magnetic field. An advantage about this observable is that one can extract 3D information about the GMF when using multiple stars in a given direction. The disadvantage is very limited sampling so it is more used to study local features instead of large-scale GMF [20].

Faraday rotation measures (RM)
The Faraday rotation measures can probe the $B_{||}$ direction and strength of the magnetic field [20]. When a linearly polarized electromagnetic wave of wavelength λ propagates through

magnetized plasma, their polarization plane changes. The RM relates the rotated angle χ to its intrinsic polarization angle χ_0 via:

$$\chi(\lambda) = \chi_0 + \text{RM} \cdot \lambda^2 \tag{12}$$

So multi-frequency observations allow one to measure the value of RM [21]. RM is then given by

$$\text{RM} = -C_{\text{RM}} \int_0^\infty n_e(\boldsymbol{x}(r)) \boldsymbol{B}(\boldsymbol{x}(r)) \boldsymbol{u}_r dr \tag{13}$$

where the observer is at the origin $\boldsymbol{x}_0$ and the positive unit vector $\boldsymbol{u}_r$ is pointing away from the observer. $\boldsymbol{B}$ is the magnetic field vector at a position $\boldsymbol{x}(r) = \boldsymbol{x}_0 + \boldsymbol{u}_r \cdot r$. Furthermore, n_e is the density of the thermal electron plasma in the interstellar medium and C_{RM} is a constant given by $C_{\text{RM}} \approx 0.8119 (\text{rad m}^{-2})(\text{cm}^3 \text{pc}^{-1} \mu\text{G})$ [4]. A negative RM implies a field pointed away from the observer.

With Equation (13) the RM yields the regular magnetic field averaged over large volume. However, that gets more complicated in a turbulent medium where the fluctuations in magnetic field and electron density contribute to RM. The magnetic field can be correlated or anti-correlated with the electron density leading to an overestimation or underestimation, respectively. The relation between the uncorrelated rotation measure RM_0 and the general case RM is given by: [22]

$$\text{RM} = \text{RM}_0 \left(1 + \frac{2}{3} \kappa \frac{\langle b^2 \rangle}{\overline{B}^2 + \langle b^2 \rangle} \right) \tag{14}$$

where κ is the correlation coefficient. The magnetic field $\boldsymbol{B} = \overline{\boldsymbol{B}} + \boldsymbol{b}$ is split into the regular coherent field ($\overline{\boldsymbol{B}}$) and the turbulent random parts ($\boldsymbol{b}$) and the angular brackets denote averaging.

Diffuse polarized synchrotron emission

The diffuse polarized synchrotron emission can probe the $B_\perp$ strength and orientation [20]. It originates from cosmic-ray electrons and positrons spiraling due to the coherent magnetic field of the Galaxy [4]. The relationship between the synchrotron volume emissivity j_ν and the magnetic field strength $B_\perp$ depends on the energy distribution of cosmic-ray electron $n_{cre}(E)$. If n_{cre} is following a power law $n_{cre}(E) = n_0 E^{-p}$ we have:

$$j_\nu \propto n_0 \nu^{\frac{-(p-1)}{2}} B_\perp^{\frac{p+1}{2}} \tag{15}$$

where the parameter p can be approximated with $p \approx 3$ [4].

When n_{cre} does not follow a power law we need to obtain the local volume emissivity at position $\boldsymbol{x}$ by integrating the single-electron emissivity $j(E, B_\perp(\boldsymbol{x}))$ multiplied by n_{cre} over energy [4]:

$$j_\nu(\boldsymbol{x}) = \int_0^\infty j(E, B_\perp(\boldsymbol{x})) n_{cre}(\boldsymbol{x}, E) dE. \tag{16}$$

With given $n_{cre}(\boldsymbol{x}, E)$ and $B_\perp(\boldsymbol{x})$ the integral over the emissivities along the line of sights yields

the Stokes parameters Q and U of the PI [4]. Every polarization of light can be described using four Stokes parameters. Q and U are the two parameters describing linear polarization and they are related to PI via:

$$\text{PI}^2 = Q^2 + U^2 \tag{17}$$

Q and U can be used to probe strength and orientation of the magnetic field. The line-of-sight average of the n_{cre}-weighted magnetic field angle in the plane of the sky is given by: [4]

$$\langle \psi_{mag} \rangle = \psi_{PA} + \pi/2 = \frac{1}{2} \arctan(U/Q) + \pi/2 \tag{18}$$

where ψ_{PA} is the observed polarization angle.

4 Unger-Farrar Model

The new model for a coherent magnetic field of the Milky Way by Michael Unger and Glennys R. Farrar [4] (UF23) consists of a set of eight models describing the global structure of the field. The following section summarises the paper [4] and presents the different magnetic field components that are implemented into gammaALPs (Section 5.2).

The GMF was derived by fitting parametric models to the two astrophysical data sets Faraday rotation measures and polarized intensity of synchrotron emission (see section 3.1).
The data set of RMs included in total 53 773 RMs. After removing multiple measurements of the same extragalactic object and rejecting outliers, 44 857 RMs were left. They were reduced to the final 41 686 RMs by excluding lines of sight where they pass through magnetized objects with a large angular size (like the Andromeda Galaxy (M31) or the Magellanic Clouds) and where they pass through H II regions. The final RMs were then binned in 3072 angular pixels with an angular diameter of 3.7° on a skymap. This lead to 2838 pixels with RM data that were used in the modelling of the GMF.
For the polarized synchrotron emission, data was provided by the Wilkinson Microwave Anisotropy Probe (WMAP) and Planck satellites. From WMAP, the data of the final 9 years of the polarized synchrotron emission at 22.5 GHz and from Planck the third release of the polarized synchrotron foreground at 30 GHz was used. For modelling the GMF, some regions with strong local features were masked out, like the regions of high PI along the Galactic plane and the north polar spur and regions with strong extragalactic sources such as the radio lobes of Centaurus A. Additionally, high-latitude polarized emission at $90° < l < 180°$ and large circular arcs visible in PI were removed. That leaves 57.8 % of the sky for analysis. One of the eight models (synCG) uses a combined analysis of WMAP and Planck data presented by the COSMOGLOBE Collaboration [23] as an alternative to the analysis by Unger and Farrar.
In addition to the RM and PI data, auxiliary models of the thermal electron density (n_e) and the cosmic-ray electrons (n_{cre}) were necessary. Two of the eight models use the NE2001 model of Cordes & Lazio [24] and the other six use the newer YMW16 model of Yao et al. [25] (see

Model	Disk	Toroidal	Poloidal	n_e Model	κ (n_e)	h_D (n_{cre})	QU	χ^2/ndf
base	GD	Explicit	CX-sigm	YMW16	0	6	(W+P)/2	1.22
expX	GD	Explicit	CX-expo	YMW16	0	6	(W+P)/2	1.30
spur	LS	Explicit	CX-sigm	YMW16	0	6	(W+P)/2	1.23
neCL	GD	Explicit	CX-sigm	NE2001	0	6	(W+P)/2	1.19
twistX	GD	Twisted	CX-sigm	NE2001	0	6	(W+P)/2	1.26
nebCor	GD	Explicit	CX-sigm	YMW16	-0.4	6	(W+P)/2	1.22
cre10	GD	Explicit	CX-sigm	YMW16	0	10	(W+P)/2	1.22
synCG	GD	Explicit	CX-sigm	YMW16	0	6	CG	1.50

Table 1: Eight selected GMF models, that have been implemented into gammaALPs. GD: grand-design spiral (Section 4.1.1), LS: local spur (Section 4.1.2), CX: coasting X-field (Section 4.1.4), κ: correlation coefficient (see Equation 14), (W+P)/2: WMAP and Planck average, CG: COSMOGLOBE

Table 1). The two models differ regarding the positions and width of the spiral arms, the density in the molecular ring, and the scale height of the thick disk of the warm ionized medium.

For the density distribution of cosmic ray electrons, the DRAGON plain diffusion model (DPD) was used. For varying half-heights h_D of the diffusion volume approximated as a cylinder, the cosmic-ray diffusion equation were solved with the DRAGON program from Evoli et al. [26]. The half-height h_D was considered to be 2, 4, 6, 8, and 10 kpc, but of the final 8 models one has $h_D = 10$ kpc and the other 7 have $h_D = 6$ kpc (see Table 1).

4.1 The UF23 Model

The UF23 model describes the global structure of the GMF as a superposition of different components. One component is the disk field, a logarithmic spiral beyond a minimum radius, that can be described as a grand-design Fourier spiral, or a single local spiral spur. The other component is a large-scale halo field that is composed of a toroidal and poloidal field, which can be described separately or by a unified halo model with a twisted-X field.

4.1.1 Fourier Spiral Disk

The Fourier spiral is a new description of the spiral arms of the galactic disk, that avoids discontinuities. The magnetic field in cylindrical coordinates at position (r, ϕ, z) is given by:

$$\boldsymbol{B}_d = (\sin\alpha, \cos\alpha, 0)\frac{r_0}{r}B(r_0, \phi_0)h_d(z)g_d(r) \qquad (19)$$

where α is a fix pitch angle, r_0 is a reference radius with $r_0 = 5$ kpc, $B(r_0, \phi_0)$ is the magnetic field strength as a function of the angle ϕ_0 at the reference radius r_0, and $h_d(z)$ and $g_d(r)$ describe the fade-in and fade-out of the field in the vertical (z) and radial (r) direction, respectively. The magnetic field strength is decomposed at the reference radius r_0 into n modes of strength B_m and phase ϕ_m. The analysis showed, that the optimal number of modes $n = 3$ is:

$$B(r_0, \phi_0) = \sum_{m=1}^{3} B_m \cos\left(m(\phi_0 - \phi_m)\right) \tag{20}$$

where ϕ_0 is determined through:

$$\phi_0 = \phi - \ln\left(\frac{r}{r_0}\right) / \tan \alpha \tag{21}$$

for given coordinates (r, ϕ).

The fade-in and fade-out function are given by:

$$h_d(z) = 1 - \sigma\left(\frac{|z| - z_d}{w_d}\right) \tag{22}$$

and

$$g_d(r) = \left[1 - \sigma\left(\frac{r - r_2}{w_2}\right)\right] \sigma\left(\frac{r - r_1}{w_1}\right) \left(1 - e^{-r^2}\right) \tag{23}$$

where $\sigma(x)$ is the logistic sigmoid function:

$$\sigma(x) = \frac{1}{1 + e^{-x}}. \tag{24}$$

The sigmoid function suppresses the disk field to half of its value at transition height z_d, inner radius r_1 and outer radius r_2, and the suppression rate is given by the corresponding transition widths w_i. For consistency with the YMW16 model the inner and outer radius are fixed to $r_1 = 5$ kpc and $r_2 = 20$ kpc. The radial transition widths are fixed to $w_1 = w_2 = 0.5$ kpc and the vertical parts z_d and w_d are free parameters.

These formulas for a Fourier spiral result in a smooth disk field without discontinuities. For a visual representation, see Figure 3 in Section 5.2.

4.1.2 Spiral Spur Disk

Instead of the grand-design Fourier spiral, one of the final models uses an isolated magnetic spiral spur in the disk, that can describe the data equally well. The magnetic field has a similar form to Equation (19):

$$\boldsymbol{B}_S = (\sin \alpha, \cos \alpha, 0) \frac{r_0}{r} B(r_0, \phi_0) h_d(z) g_S(\phi) \tag{25}$$

h_d is again given by Equation (22), but instead of the Fourier sum, the strength is modelled as a Gaussian of width w_s at a reference radius r_0:

$$B(r_0, \phi_0) = B_1 \exp\left(-\frac{1}{2}\left(\frac{\phi_0 - \phi_1}{w_s}\right)^2\right) \tag{26}$$

where B_1 is the magnetic field strength (a free parameter), the angle ϕ_1 denotes the center of the spur and ϕ_0 follows via Equation (21). Instead of the radial fade-out function $g_d(r)$, Equation (25), uses a fade-out function depending on the angle ϕ:

$$g_s(\phi) = 1 - \sigma\left(\frac{\Delta(\phi, \phi_c) - L_c}{w_c}\right) \tag{27}$$

where $\sigma(x)$ is again the sigmoid function (Equation (24)), ϕ_c is the angular center of the spur, L_c is the angular half-length and $\Delta(\phi, \phi_c) = |\phi_c - \phi|$ so that the magnetic field is suppressed to half its value at $\phi = \phi_c \pm L_c$.

The reference radius is fixed to $r_0 = 8.2$ kpc (position of the sun) and the transition width is fixed to $w_c = 5°$. For a visual representation, see Figure 3 in Section 5.2.

4.1.3 Toroidal Halo

The toroidal field uses the same ansatz as the "jansson12" model ([27]). It is purely azimuthal, so it only has a ϕ component in cylindrical coordinates:

$$\boldsymbol{B}_t = (0, 1, 0) \cdot (1 - h_d(z)) e^{-\frac{|z|}{z_t}} \left(1 - \sigma\left(\frac{r - r_t}{w_t}\right)\right) B_{N/S} \tag{28}$$

$h_d(z)$ is defined in Equation (22), so the toroidal field is phased in by the complement of the function that phases out the disk field. The exponential scale height z_t, the transition radius r_t, the transition width w_t and the maximum magnetic field strength $B_{N/S}$ are all free parameters, where $B_{N/S}$ is split into northern and southern magnetic field strength:

$$B_{N/S} = \begin{cases} B_N & z > 0 \\ B_S & \text{otherwise} \end{cases} \tag{29}$$

The toroidal field has opposite sign above and below the disk, see Figure 4.

4.1.4 Poloidal Halo

In addition to the purely azimuthal toroidal halo field a poloidal "X-field" is implemented:

$$\boldsymbol{B}_p = (B_r, 0, B_z) \tag{30}$$

11

For this poloidal halo field, a power-function X-field and a coasting X-field were tested. The eight final models, that are implemented into gammaALPs, use the coasting X-field with parallel field lines beyond a certain reference radius a_c. The radial and vertical components at position (r, ϕ, z) are given by:

$$B_r = B_0(a) \frac{a^2 a_c^p z |z|^{p-2}}{r z_p^p \sqrt{\Delta^2 + 4a_c^p r^p}} \tag{31}$$

and

$$B_z = B_0(a) \left(\frac{r}{a}\right)^{p-2} \frac{a^p + a_c^p}{\sqrt{\Delta^2 + 4a_c^p r^p}} \tag{32}$$

The coasting radius a_c, the field line exponent p and the scale height z_p are free parameters. The radius a is given by:

$$a = \frac{2a_c^p r^p}{\sqrt{\Delta^2 + 4a_c^p r^p} + \Delta} \tag{33}$$

and Δ is:

$$\Delta = a_c^p + \left(\frac{a_c |z|}{z_p}\right)^p - r^p \tag{34}$$

For the magnetic field strength $B_0(a)$ different radial functions were tested. Of the final 8 models, 7 use the logistic sigmoid:

$$B_0(a) = B_p \left(1 - \sigma\left(\frac{a - r_p}{w_p}\right)\right) \tag{35}$$

And one uses an exponential function:

$$B_0(a) = B_p e^{-\frac{a}{r_p}} \tag{36}$$

This poloidal halo model improves the X-field model in JF12 by getting rid of discontinuities in the inner galaxy and at the galactic plane. An example of the X-field can be seen in Figure 5 in Section 5.2.

4.1.5 Unified Twisted Halo

Instead of a separate toroidal halo field, one could describe the entire halo in a unified model. The toroidal halo field can be the result of differential rotation of the poloidal halo field. The differential rotation of the Galaxy would create a toroidal field with opposite directions in the northern and southern hemisphere. The magnetic field of one possible model based on this idea is given by:

$$\boldsymbol{B}_H = (B_r, B_\phi(t), B_z) \tag{37}$$

where B_r and B_z are given by Equation (31) and Equation (32) and the evolution of the azimuthal field is given by:

$$B_\phi(t) = (B_z \Delta_z + B_r \Delta_r)t \tag{38}$$

12

with the twisting time t and with the two shear terms

$$\Delta_z = -\text{sgn}(z)\frac{v_0}{z_v}\left(1 - e^{-r/r_v}\right)\frac{4e^{2|z|/z_v}}{\left(1 + e^{2|z|/z_v}\right)^2} \tag{39}$$

and

$$\Delta_r = v_0\left(\frac{e^{-r/r_v}}{r_v} - \frac{1 - e^{-r/r_v}}{r}\right)\frac{2}{1 + e^{2|z|/z_v}} \tag{40}$$

where the galactic rotation velocity $v_0 = -240$ km s^{-1}, the scale height of the rotation curve $z_v = 10$ kpc and the scale radius of the rotation curve $r_v = 1.6$ kpc are fixed parameters.

An example of the twisted X-field can be seen in Figure 2. The twisting process cannot continue over the entire lifetime of the galaxy because the azimuthal field strength would get too big. However, this model describes the magnetic field at the current point of time, so the twisting time t was considered a free parameter that was fit to $t = 54.7 \pm 1.1$ megayears in the "twistX" model.

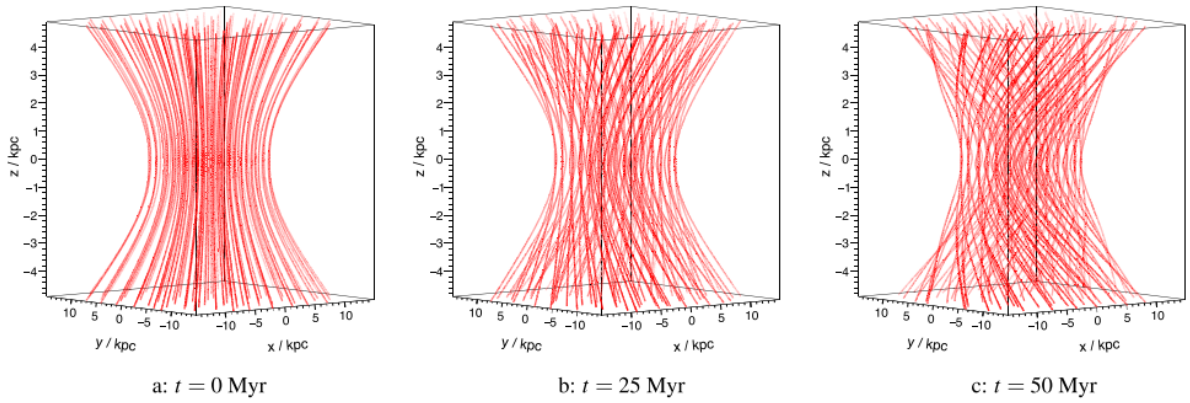a: $t = 0$ Myr   b: $t = 25$ Myr   c: $t = 50$ Myr

Figure 2: Illustration of the twisted X-field in the unified halo model at different times $t = 0$, 25, and 50 megayears, from [4] page 13.

5 Implementation of UF23

The objective of this Bachelor thesis was to implement the magnetic field model (UF23) that I described in Section 4.1, into the python package gammaALPs. The following section will give an overview of gammaALPs, then describe how the UF23 model is implemented, show some applications and how to work with the new model, and then discuss the effect of the new model on photon-ALP mixing.

5.1 gammaALPs

The python package gammaALPs is an open-source code that calculates the oscillation probability between photons and axion-like particles (ALPs) in different astrophysical environments (code:[28], paper: [19]). The source code is hosted on GitHub[1] and instructions on installation and requirements can be found in the documentation[2]. It is based on the python packages numpy [29], scipy ([30]), astropy ([31], [32], [33]), and numba ([34]).

The gammaALPs code calculates the conversion probability by solving the equations of motion for photon-ALP oscillation using transfer matrices (see Section 2.3). When the photon-ALP beam travels from the source to the observer it can pass through several magnetic field environments. The user can initialize their own environment from a file or an array, but there are also many possible environments already implemented into gammaALPs.

Starting at the source, there are two models of active galactic nuclei (AGN) jets. One of the models considers a coherent toroidal magnetic field, and the other model considers a helical component (transforming from toroidal to poloidal) and a tangled component in the magnetic field of the AGN jet.

After the source, there are three environments for mixing in the intracluster medium (ICM). One where the magnetic fields follows a cell-like structure, one magnetic field with Gaussian turbulence, and the third one where the magnetic field is assumed to follow a structured field.

Then there is one environment for the intergalactic magnetic field (IGMF) also based on a cell-like structure that includes γ-ray absorption on the extragalactic background light (EBL).

And at the end, there are two possible models for the magnetic field of the milky way: The model by Jansson and Farrar [27], which also has two additional options for modification with Planck data [35], and the model by Pshirkov et al. [21] with the option for an axissymmetric or bisymmetric model.

Now, in addition to these two models, it was my task to implement the new model for the coherent magnetic field of the milky way by Michael Unger and Glennys R. Farrar into gammALPs.

---

[1]https://github.com/me-manu/gammaALPs
[2]https://gammaalps.readthedocs.io

5.2 UF23 Model in gammaALPs

The new UF23 model for the magnetic field is currently hosted on a forked repository [3] at the branch gmf-unger-farrar. It was created similar to the existing C++ code by Unger and Farrar [36] and the calculations of the python implementation were compared to the C++ code for 35301 sample points for each model and they all matched.

The model is implemented as a python class, that contains eight methods. When creating an instance of the class one can choose between the eight models listed in Table 1 by passing the model name as an argument, the default is the "base" model. Based on the chosen model the `__init__()` method sets the free model parameters to the fitted value (see Table 3 in [4]). The five methods `spiral_field`, `spur_field`, `toroidal_halo_field`, `poloidal_halo_field` and `twisted_halo_field` calculate the magnetic field for the different components according to the formulas described in Section 4.1. The two methods for the disk field take three N-dimensional numpy arrays as input for the positions in cylindrical coordinates (ρ, ϕ, z) (see Listing 1). The methods for the halo field only take two N-dim numpy arrays for ρ and z. The arrays need to have the same shape. The functions then return a tuple containing the magnetic field as a (3,N)-dimensional array with (ρ, ϕ, z) components and also the absolute value of the magnetic field for each coordinate tuple as a N-dimensional array, all in units of μG.

The methods `Bdisk` and `Bhalo` are then used within gammaALPs. If the chosen model is the "spur" model, the `Bdisk` method returns the return of the `spur_field` or else the return of the `spiral_field`. The `Bhalo` method similarly returns the return of the `twisted_halo_field` for the "twistX" model or else the sum of the `toroidal_halo_field` and the `poloidal_halo_field`.

The UF23 class can be used with gammaALPs as an environment to calculate photon-ALP oscillation (see Section 5.3), but it can also be accessed separately to work with the magnetic field. A short example is shown in Listing 1.

```python
from gammaALPs.bfields import gmf # contains the UF23 class
import numpy as np

# create numpy arrays with the positions you want to calculate the b-
    field for, for example
x = np.array([-10, -5, 0, 5, 10])
y = np.array([-12, -7, 0, 7, 12])
z = np.array([-4, -2, 0, 2, 4])

# input for calculation needs to be in cylindrical coordinates
r = np.sqrt(x**2 + y**2)
phi = np.arctan2(y, x)

# initialize the GMF model
uf23 = gmf.UF23(model='base')
```

---

[3] https://github.com/FriedL12/gammaALPs

```
16  # calculate the total magnetic field for the 5 positions
17  b_vec = uf23.Bdisk(rho=r, phi=phi, z=z)[0] + uf23.Bhalo(rho=r, z=z)[0]
18  b_abs = uf23.Bdisk(rho=r, phi=phi, z=z)[1] + uf23.Bhalo(rho=r, z=z)[1]
19
20  # or access single component with
21  b = uf23.toroidal_halo_field(rho=r, z=z)
```

Listing 1: Example UF23 access

In this example `b_vec` would be a (3, 5)-dimensional array containing 5 magnetic field vectors. The magnetic field for the position (-10, -12, -4) would be given by `b_vec[:,0]`, the variable `b_abs` contains an array of shape (5,) with the absolute value of the magnetic field at the five positions, and `b` is a tuple containing the magnetic field vectors for the toroidal field in a (3, 5)-dimensional array and the magnetic field strength for these five vectors in an array.

This access to the GMF class can then be used to plot the different magnetic field components. Figure 3 shows the disk field for all 8 models. The first seven models use the Fourier-spiral component and only differ in the fitted parameters (see Table 3 in [4]). The "spur" model uses the spur field and only models one of the "galaxy-arms".

The toroidal halo fields are shown in Figure 4 and the poloidal halo fields are shown in Figure 5. An illustration of the unified model was given in Figure 2.
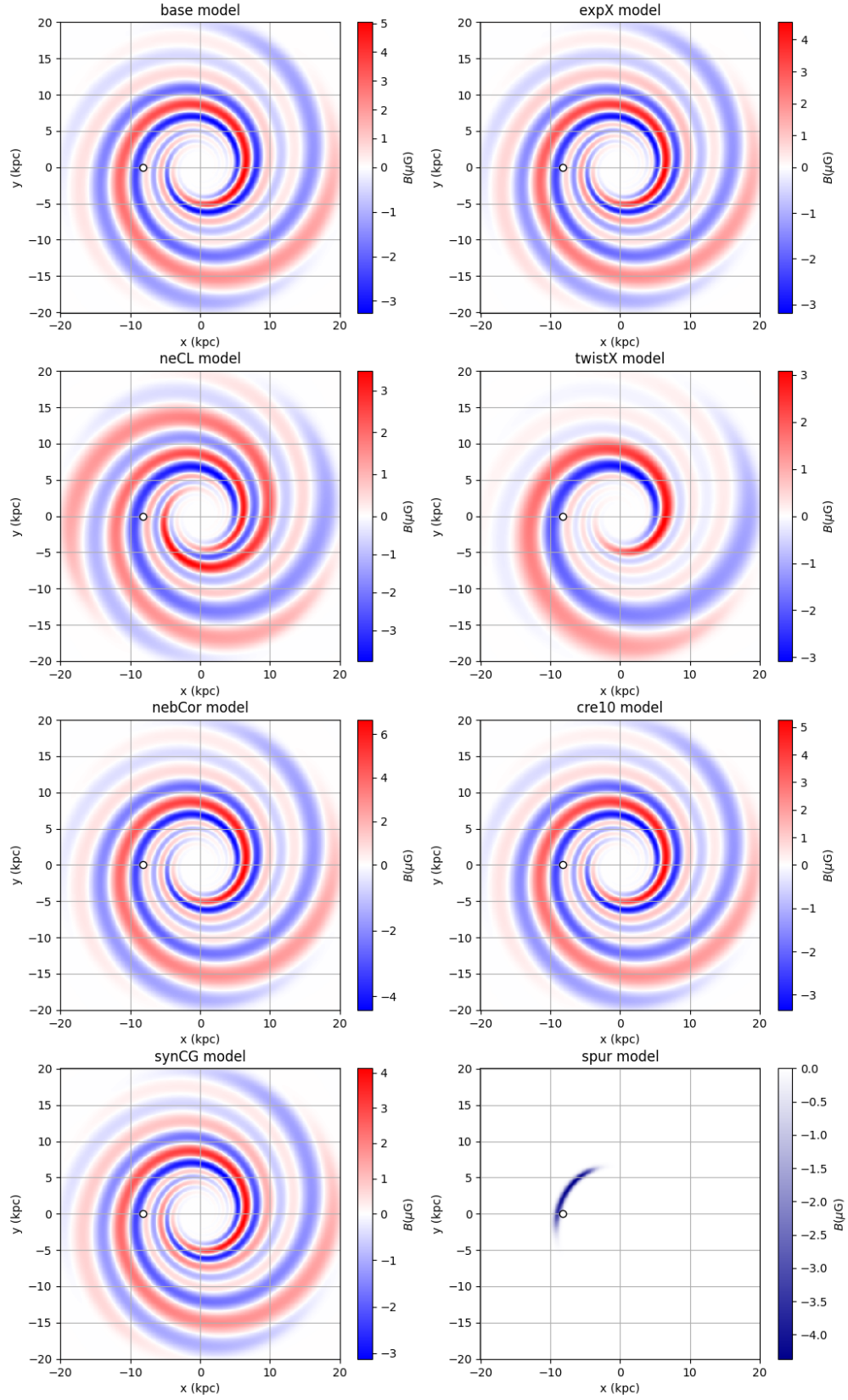
Figure 3: Magnetic field disks for all eight models (see Table 1) at $z = 0$, for red the magnetic field is pointing counterclockwise, for blue clockwise. The white point marks the position of our sun.
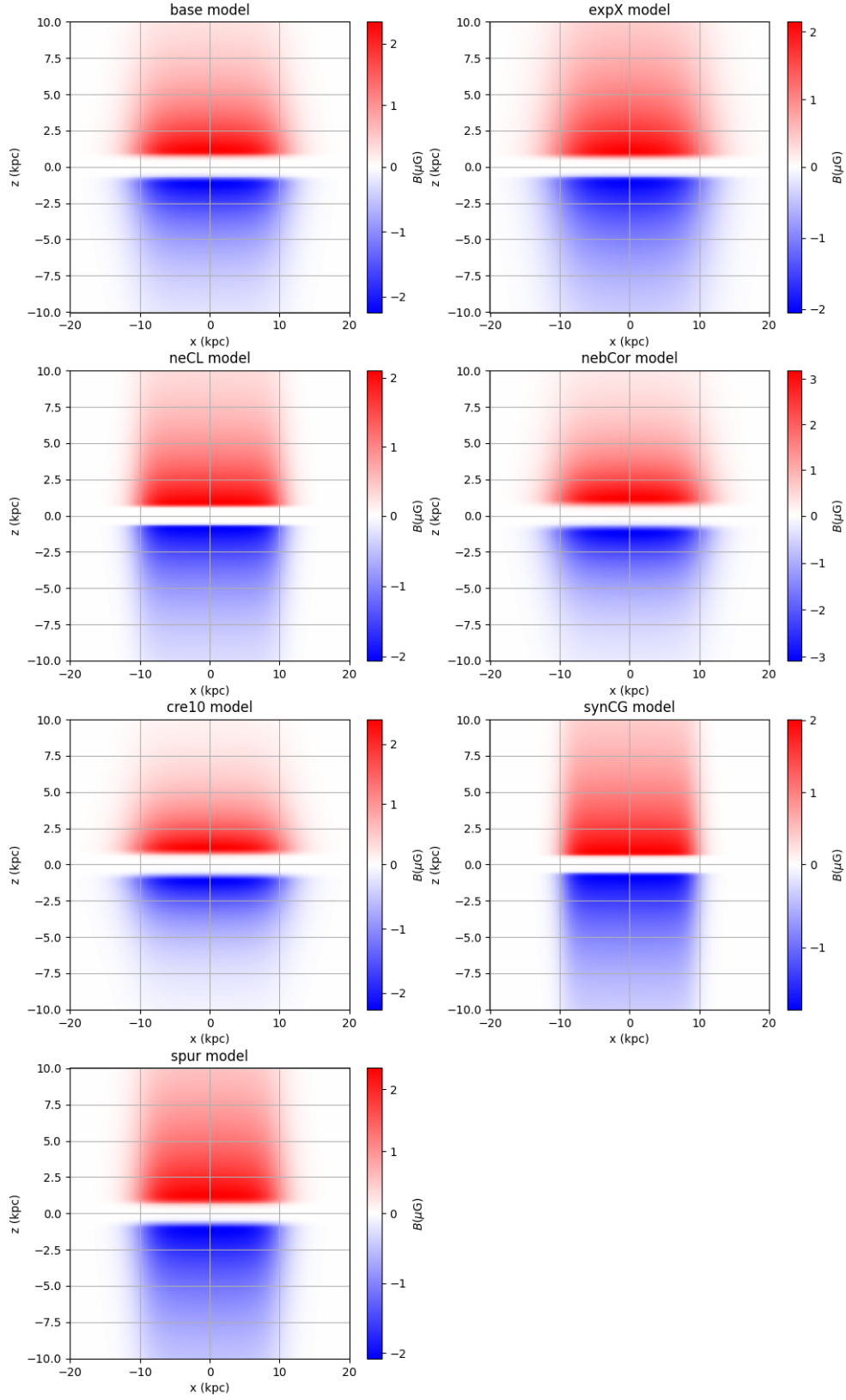
Figure 4: Toroidal component of magnetic halo field for all models except the unified halo ("twistX") at $y = 0$. Red is counterclockwise and blue is clockwise pointing magnetic field when looking from positive z to negative z.
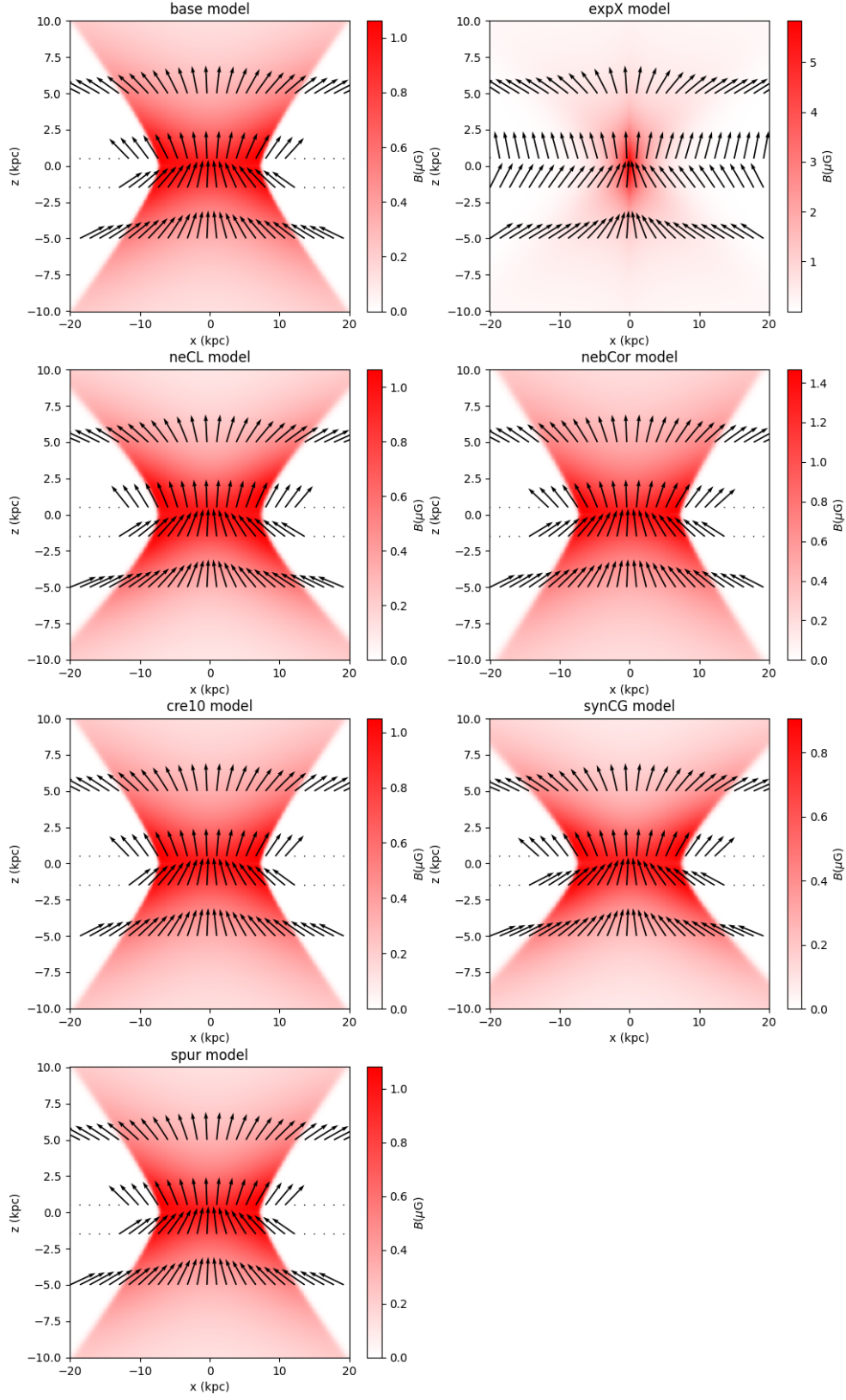
Figure 5: Poloidal component of magnetic halo field for all models except the unified halo ("twistX") at $y = 0$.

5.3 Applications

The newly implemented UF23 model can now be used as an environment for calculations of photon-ALP oscillation. Listing 2 shows an example for the calculation of the conversion probability with the new magnetic field model.

```python
from gammaALPs.core import Source, ALP, ModuleList
import numpy as np

# define a source
src = Source(z=0.02, l=12., b=12.)

# define the ALP
m = 1. # mass in neV
g = 0.5 # coupling in 1e-11 GeV^-1
alp = ALP(m, g)

# define the energy range in GeV
EGeV = np.logspace(-1., 3., 101)

# define initial polarization matrix
pa_in = np.diag([0., 0., 1.]) # pure ALP state

# initialize the module list
ml = ModuleList(alp, src, pin=pa_in, EGeV=EGeV)

# add environments to module list
ml.add_propagation("GMF", 0, model="UF23", UF23_model="base")

# calculate conversion probability as a function of energy
px, py, pa = ml.run()

# total conversion probability is
pag = px + py
```

Listing 2: Example UF23 application

After importing the necessary modules, the source has to be defined. The position of the source can be defined with the redshift z the longitude l and latitude b in galactocentric coordinates. Instead of l and b the user can define the position in equatorial coordinates with the right ascension "ra" and declination "dec". When the source has been defined in galactocentric coordinates, the equatorial coordinates can be accessed with src.ra and src.dec. Next, the ALP class is initialised with a mass in neV and the coupling constant in 10^{-11} GeV. Those parameters will be used for the calculations. Then the energy range has to be set and the initial polarization matrix has to be defined. In the example (Listing 2), only the mixing in the magnetic field of the milky way is considered, so the initial polarization matrix is set to a pure ALP beam. With all the defined parameters and objects, the module list is initialised. The module list will con-

tain all the environment the photon-ALP beam will travel through. With `add_propagation`, an environment is added to the module list. If multiple environments are added, the index (in this example 0) defines the position, where 0 is the closest to the source. When all propagation environments are added, the final photon and ALP polarization states are calculated with `ml.run()`. The total conversion probability is then given by the sum of the final photon states. The conversion probability of the example is shown in Figure 6 as a function of energy. It can also be calculated as a function of distance as shown in Figure 7. In addition to the conversion probability, the perpendicular component of the magnetic field is plotted. The conversion probability at $r = 0$ kpc corresponds with the entry into the magnetic field environment and at maximum r, the observer is located.
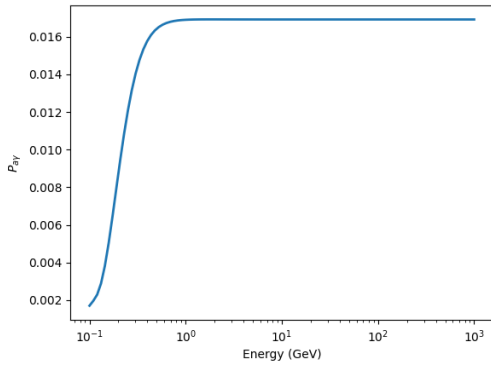

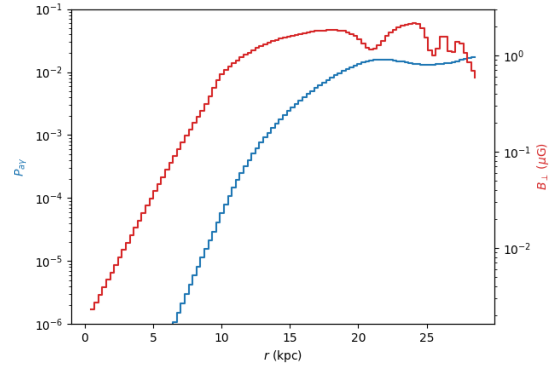Figure 6: Conversion probability as a function of energy for the example in Listing 2

Figure 7: Conversion probability as a function of distance traveled in magnetic field at energy $E = 3.98$ GeV (blue, left axis) and perpendicular component of magnetic field (red, right axis)

Next, the calculations of conversion probability can be used to create full sky maps. The skymaps are created with the help of the healpy and HEALPix[4] package [37]. For each pixel in the sky map a new source is defined and similar to the example in Listing 2 the conversion probability is calculated at one single energy (1 GeV). Figure 10 shows the sky maps for all eight new models. Figure 8 is a bigger picture for the base model and, for comparison, Figure 9 shows the sky map for the older jansson12 model. The calculation uses an axion mass of $m = 10$ neV and a coupling constant of $g_{a\gamma} = 0.5 \cdot 10^{-11}$ GeV^{-1}.

All eight new models show a similar asymmetry in longitude, which is the result of the twisted nature of the halo field, but they also show differences in the conversion probability. Especially the "expX" and "nebCor" model show a high conversion probability near the center. That is the result of a higher magnetic field in these two models. This could also be seen in the plots of the magnetic field components (Figure 3, 4 and 5). The sky map for the old "jansson12" model shows obvious differences in the shape. The following Section 5.4 compares the results of the new "base" and "neCL" model with the two older models "jansson12" and "pshirkov".

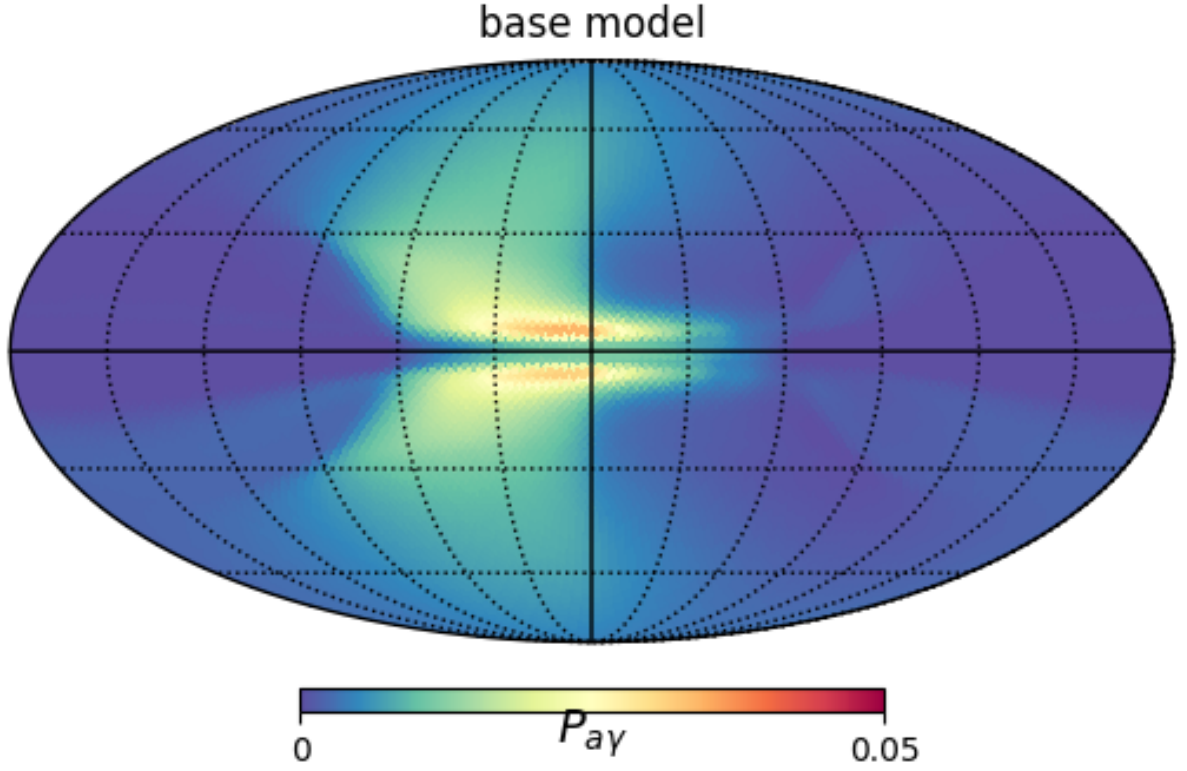[4] http://healpix.sourceforge.net

base model

Figure 8: Conversion probability sky map for the "base" model at Energy $E = 1$ GeV, axion mass $m = 10$ neV and coupling constant $g_{a\gamma} = 0.5 \cdot 10^{-11}$ GeV^{-}1
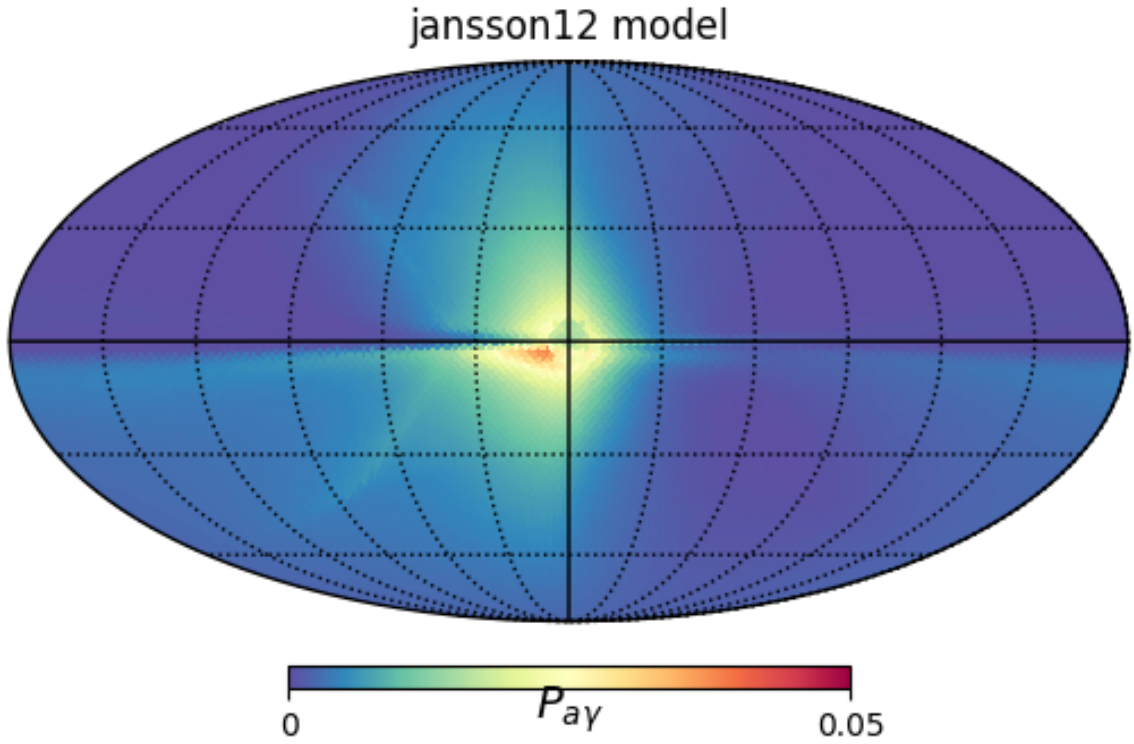

jansson12 model

Figure 9: Conversion probability sky map for the "jansson12" model at Energy $E = 1$ GeV, axion mass $m = 10$ neV and coupling constant $g_{a\gamma} = 0.5 \cdot 10^{-11}$ GeV^{-}1
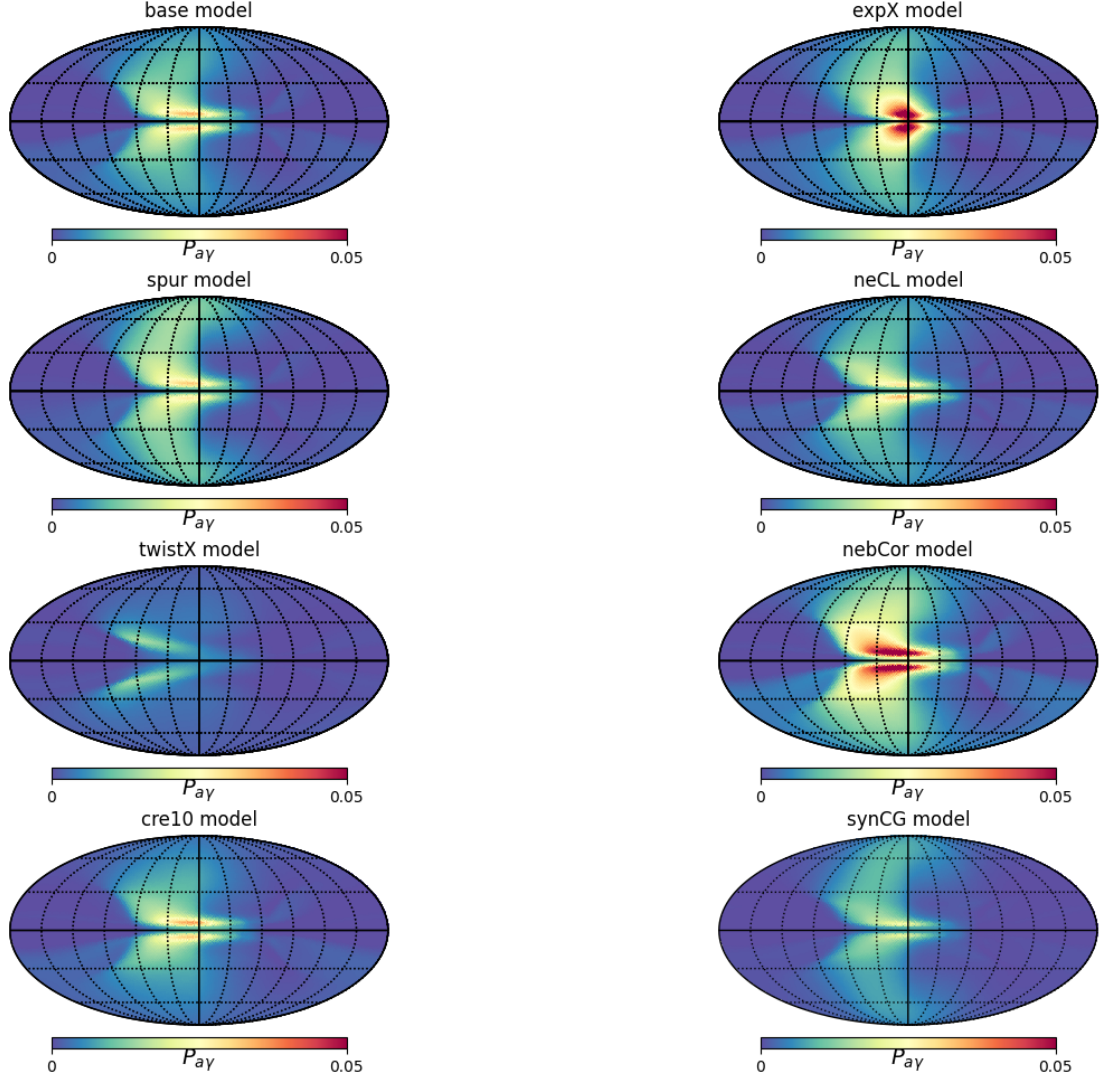
Figure 10: Conversion probability sky maps for the eight new models at Energy $E = 1$ GeV, axion mass $m = 10$ neV and coupling constant $g_{a\gamma} = 0.5 \cdot 10^{-11}$ GeV^{-1}

5.4 Effect on photon-ALP mixing

The differences between the new UF23 model and the older jansson12 and pshirkov model will be analysed with two example γ-ray sources. The first γ-ray source is NGC 1275, also known as Perseus A. NGC 1275 is a radio galaxy at the center of the Perseus cluster, for which rotation measures suggest a high central magnetic field, and it's γ-ray spectrum was observed with the Fermi Large Area Telescope (LAT) [38]. The analysis by the Fermi-LAT collaboration gave strong constraints for the axion masses between 0.5 neV and 20 neV [38]. I will use the source to show the effect of the new UF23 model on photon-ALP mixing compared to the older models. Therefore I used similar code like the example in Listing 2 to calculate

the conversion probabilities for different masses. The position of NGC 1275 (source) is $z = 0.017559$, ra $= 3^\text{h}19^\text{m}49.9^\text{s}$, dec $= +49°30^\text{m}49.2^\text{s}$, and the energy range is 100 MeV to 1000 GeV which includes the Fermi-LAT energy range used in the analysis from 100 MeV to 500 GeV [38]. As the initial polarization a pure ALP state is assumed. Figure 11 shows in the left column the ratio of the conversion probability calculated with the "jansson12" (JF12) model and the conversion probability calculated with the new "base" model for three different masses: $m = 0.5$ neV, 10 neV and 20 neV. The right column is similar, but compares the "pshirkov" model (Pshi) to the new "base" model. The coupling constant is assumed to be $g_{a\gamma} = 0.4 \cdot 10^{-11}$ GeV^{-1}.
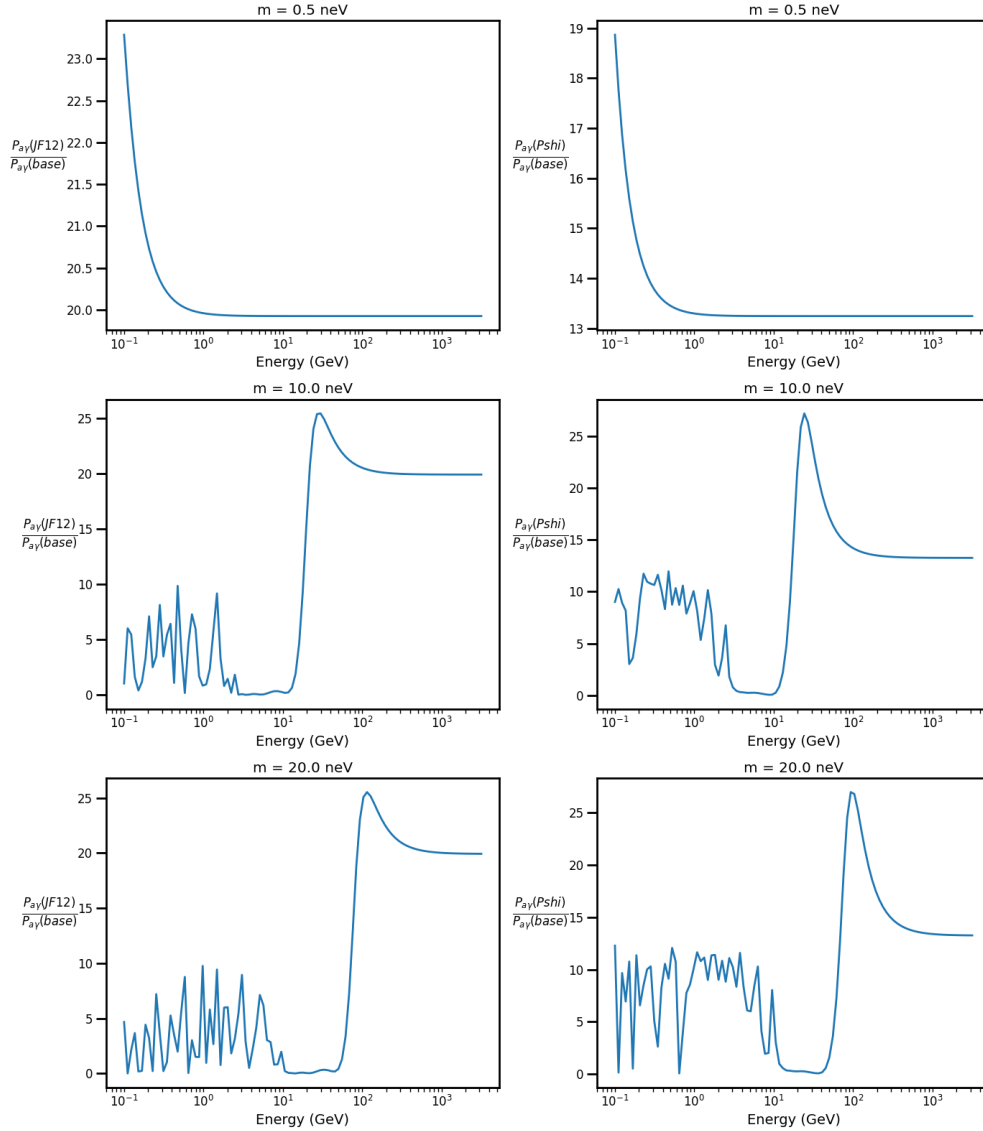

Figure 11: Ratio of the conversion probability of the two old models and the new "base" model for the NGC 1275 source for three different axion masses at an energy range similar to Fermi-LATs and a coupling constant of $0.4 \cdot 10^{-11}$ GeV^{-1}.

The plots for the "jansson12" and "pshirkov" have similar shape and only differ in the value of the conversion probability ratio. For high energy the ratio becomes constant at a value of around 20 for the "JF12" model and at around 13 to 15 for the "pshirkov" model, meaning that

the conversion probability calculated with the old models is much higher at higher energies, then the conversion probability calculated with the new model. At lower energies around 100 MeV to 3 GeV for $m = 10$ neV, and 100 MeV to 10 GeV for $m = 20$ neV the ratio fluctuates between 0 and 10. For $m = 0.5$ neV, the ratio starts with the peak and becomes directly constant. The ratio also seems constant at energies between 3 and 10 GeV for $m = 10$ neV and 10 and 50 GeV for $m = 20$ neV. In both cases the ratio is between 0.05 and 0.3, meaning $P_{a\gamma}(\text{base})$ is up to 20 times higher.

In addition to this comparison, Figure 12 also shows the conversion probability ratio, but instead of the "base" model it is the ratio with the new "neCL" model.
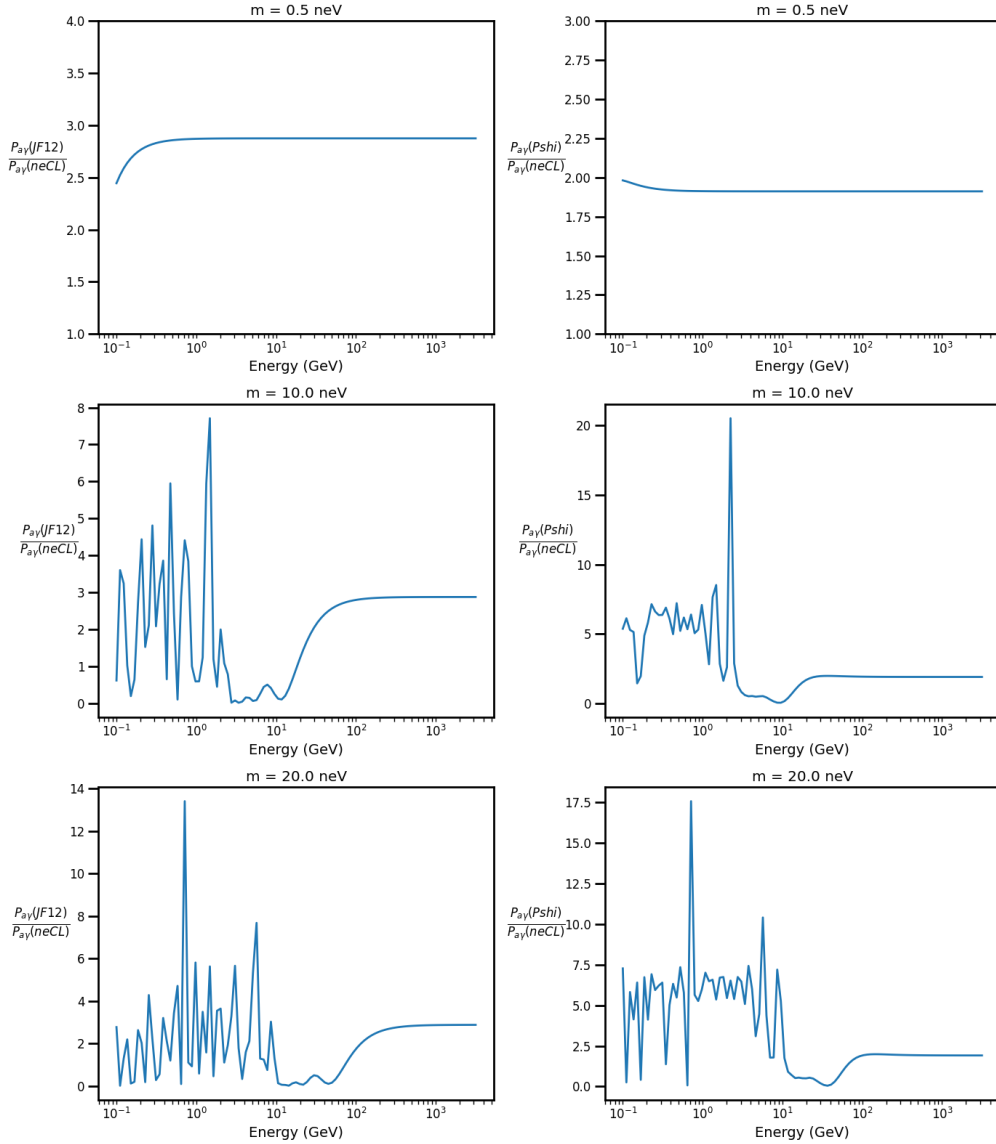

Figure 12: Ratio of the conversion probability of the two old models and the new "neCL" model for the NGC 1275 source for three different axion masses at an energy range similar to Fermi-LATs and a coupling constant of $0.4 \cdot 10^{-11}$ GeV^{-1}.

The constant ratio at higher energies is here only around 3 for the "JF12" model and 2 for the "pshirkov" model, meaning the results for the "neCL" model are much more similar to the

old models, than the "base" model is. Other than that the shapes of the ratio with the "neCL" model and with the "base" model are very similar with fluctuations at lower energies and then a constant interval in which the conversion probability of the new model is higher.

The second source is GRB 221009A that was detected by the LHAASO Collaboration [39]. GRB 221009A was a very energetic γ-ray burst with the highest photon energy reaching 18 TeV. Again using code like Listing 2 to calculate the conversion probability. The position of the γ-ray burst is ra $= 19^{\text{h}}13^{\text{m}}03.43^{\text{s}}$, dec $= +19°46^{\text{m}}23.1^{\text{s}}$ with a redshift of $z = 0.151$ [40] and the energy range is from 100 GeV to 18 TeV which includes the energy range of the LHAASO observation which was 500 GeV to 18 TeV [39]. The initial polarization is again assumed to be a pure ALP state, the coupling constant is $0.4 \cdot 10^{-11}$ GeV^{-1} and the assumed mass is for all plots is $m = 10$ neV.

Figure 13 shows the ratio of the two old models with the new "base" model and Figure 14 the ratio to the new "neCL" model.

Figure 13: Ratio of the conversion probability of the two old models and the new "base" model for the GRB 221009A source with assumed axion mass $m = 10$ neV at an energy range similar to LHAASOs and a coupling constant of $0.4 \cdot 10^{-11}$ GeV^{-1}.
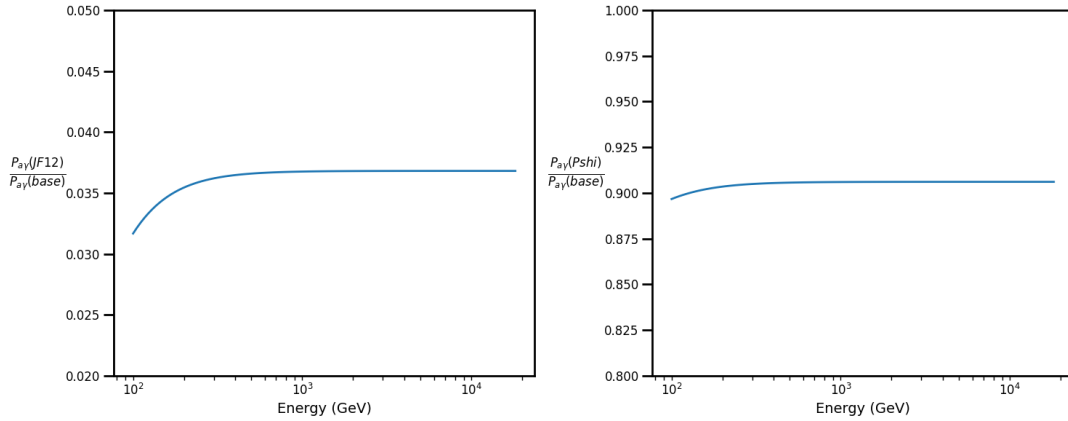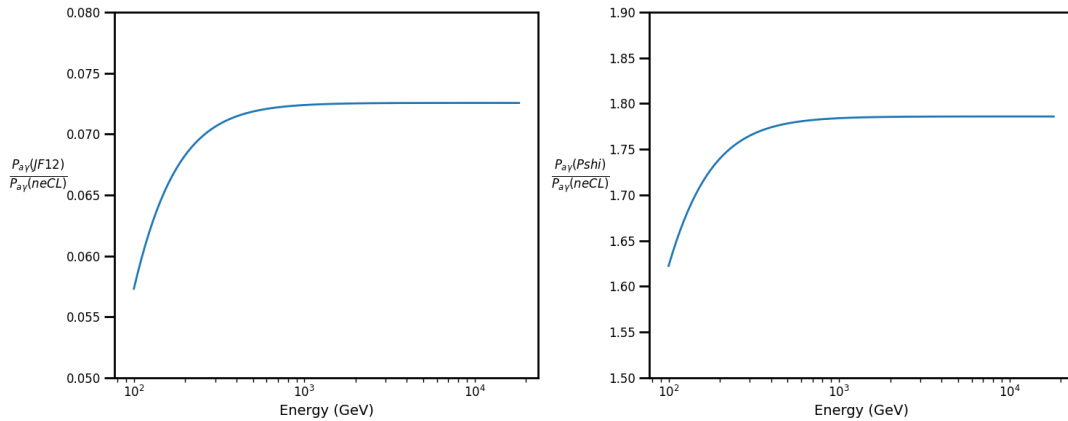

Figure 14: Ratio of the conversion probability of the two old models and the new "neCL" model for the GRB 221009A source with assumed axion mass $m = 10$ neV at an energy range similar to LHAASOs and a coupling constant of $0.4 \cdot 10^{-11}$ GeV^{-1}.

All ratios are almost constant for this high energy range, but the values differ. For the "JF12" model the ratios are constant around 0.035 ("base") and 0.07 ("neCL"). So for this source, the conversion probability calculated with the new models is up to 30 times higher than the conversion probability calculated with the "jansson12" model. The ratios for the "pshirkov" model are closer to 1, so the results for the conversion probability are similar at this energy range. The ratio $P_{a\gamma}(\text{Pshi})/P_{a\gamma}(\text{base})$ is constant around 0.9 and the ratio $P_{a\gamma}(\text{Pshi})/P_{a\gamma}(\text{neCL})$ is constant at 1.78.

These two examples show that the new UF23 model definitely has an effect on the calculation of the conversion probability. One good thing about the UF23 model is that there are 8 different models that describe the data equally well but have different fitted parameters. The difference between the "base" and "neCL" model is the electron density model that was used for fitting. The "neCL" model uses the NE2001 model [24] for fitting, which was also used for the "pshirkov" and "jansson12" model, while the "base" model uses the newer YMW16 model [25]. The different models give more opportunities to study the effect of the Milky Way magnetic field on photon-axion conversion.

6 Summary and Outlook

In this thesis, I investigated the effect of the Milky Way magnetic field on photon-axion conversion. The focus was on the new model for a coherent magnetic field of the Milky Way by Michael Unger and Glennys R. Farrar. The new model consists of eight models with different functional forms, data products, and auxiliary input (see Table 1). The model parameters are fit to Faraday rotation measures and polarized synchrotron intensity maps.

The task of this work was, to implement this new UF23 model into the python package gammaALPs, which is an open-source code to calculate the mixing of photons and ALPs in many different astrophysical magnetic field environments. After the new model was implemented, I validated it by comparing the results of the magnetic field calculations to the results of an existing C++ code by Unger and Farrar. One difference to the C++ code is the usage of numpy arrays allowing for calculation of the magnetic field at multiple coordinate points at once, and the usage of galactocentric coordinates for the entire code.

The implemented UF23 model can now be used to calculate conversion probabilities for photon-ALP beams in the environment of the Milky Way. I used the calculations to create full sky maps of the conversion probability of an incoming ALP beam (see Figure 10), and made a comparison to the two already implemented models "jansson12" and "pshirkov". For comparison I used two extragalactic γ-ray sources NGC1275 and GRB 221009A. The conversion probability calculated with the new "base" model was up to 30 times higher and lower than the one calculated with the old models (see Figure 11), while the conversion probability calculated with the new "neCL" model was much closer to the result of the old models, but also showing big fluctuations at lower energies (see Figure 12). This shows that the chosen GMF can have a big impact on the calculated conversion probabilities and for that the new UF23 model provides a set of 8 models, fit to the latest data, that can help determine the effect of different GMF uncertainties on photon-axion conversion.

In addition to the calculations for conversion probability the code for the magnetic field model can also be accessed separately and can be used for other GMF-sensitive sciences, for example cosmic-ray deflections.

For the future this new model could be used to study γ-ray spectra of astrophysical sources to put more constraints on ALP properties or even identify potential signals. However, the exact structure of the Milky Way magnetic field is still not completely understood, so the implemented model could be improved and extended in the future.

Overall, this work enhances the gammaALPs package by adding a new model for the Milky Way magnetic field that can now be used for calculations on photon-ALP mixing.

Acknowledgments

First of all, I would like to thank Prof. Dr. Manuel Meyer for providing me with this highly interesting topic for my bachelor's thesis and for taking the time for our weekly meetings to discuss my progress and the next steps.

I also want to thank Prof. Dr. Dieter Horns for agreeing to act as a supervisor for this thesis.

Then I would like to thank the entire research group for welcoming me and always being open for questions.

Furthermore I would like to thank all my friends, especially my roommate Julian, for the support and all the great times we had through our bachelor studies.

And finally, the biggest thanks goes to my family, especially my parents, for supporting me my whole life in everything I have done.

References

[1] Katherine Freese. „Status of dark matter in the universe". In: *International Journal of Modern Physics D* 26.06 (Mar. 2017), p. 1730012. URL: http://dx.doi.org/10.1142/S0218271817300129.

[2] Planck Collaboration. „Planck2018 results: VI. Cosmological parameters". In: *Astronomy & Astrophysics* 641 (Sept. 2020), A6. URL: http://dx.doi.org/10.1051/0004-6361/201833910.

[3] Manuel Meyer, Daniele Montanino, and Jan Conrad. „On detecting oscillations of gamma rays into axion-like particles in turbulent and coherent magnetic fields". In: *Journal of Cosmology and Astroparticle Physics* 2014.09 (Jan. 2017), pp. 003–003. URL: http://dx.doi.org/10.1088/1475-7516/2014/09/003.

[4] Michael Unger and Glennys R. Farrar. „The Coherent Magnetic Field of the Milky Way". In: *The Astrophysical Journal* 970.1 (July 2024), p. 95. URL: http://dx.doi.org/10.3847/1538-4357/ad4a54.

[5] Mary K. Gaillard, Paul D. Grannis, and Frank J. Sciulli. „The standard model of particle physics". In: *Reviews of Modern Physics* 71.2 (Mar. 1999), S96–S111. URL: http://dx.doi.org/10.1103/RevModPhys.71.S96.

[6] Jonathan L. Feng. „Dark Matter Candidates from Particle Physics and Methods of Detection". In: *Annual Review of Astronomy and Astrophysics* 48.1 (Aug. 2010), pp. 495–545. URL: http://dx.doi.org/10.1146/annurev-astro-082708-101659.

[7] ATLAS Collaboration. „Observation of a new particle in the search for the Standard Model Higgs boson with the ATLAS detector at the LHC". In: *Physics Letters B* 716.1 (Sept. 2012), pp. 1–29. URL: http://dx.doi.org/10.1016/j.physletb.2012.08.020.

[8] Cush (Wikipedia contributors). *Standard Model of Elementary Particles — Wikipedia, The Free Encyclopedia*. 2019. URL: https://en.wikipedia.org/wiki/File:Standard_Model_of_Elementary_Particles.svg. [Online; accessed 07-August-2024].

[9] J. M. Butterworth. „The Standard Model: how far can it go and how can we tell?" In: *Philosophical Transactions of the Royal Society A: Mathematical, Physical and Engineering Sciences* 374.2075 (Aug. 2016), p. 20150260. URL: http://dx.doi.org/10.1098/rsta.2015.0260.

[10] Gianfranco Bertone, Dan Hooper, and Joseph Silk. „Particle dark matter: evidence, candidates and constraints". In: *Physics Reports* 405.5–6 (Jan. 2005), pp. 279–390. URL: http://dx.doi.org/10.1016/j.physrep.2004.08.031.

[11] Vera C. Rubin and Jr. Ford W. Kent. „Rotation of the Andromeda Nebula from a Spectroscopic Survey of Emission Regions". In: *Astrophysical Journal* 159 (Feb. 1970), p. 379. URL: https://dx.doi.org/10.1086/150317.

[12] J. Anthony Tyson, Greg P. Kochanski, and Ian P. Dell'Antonio. „Detailed Mass Map of CL 0024+1654 from Strong Lensing". In: *The Astrophysical Journal* 498.2 (May 1998), pp. L107–L110. URL: http://dx.doi.org/10.1086/311314.

[13] Alexandre Refregier. „Weak Gravitational Lensing by Large-Scale Structure". In: *Annual Review of Astronomy and Astrophysics* 41.1 (Sept. 2003), pp. 645–668. URL: http://dx.doi.org/10.1146/annurev.astro.41.111302.102207.

[14] R. D. Peccei and Helen R. Quinn. „CP Conservation in the Presence of Pseudoparticles". In: *Phys. Rev. Lett.* 38 (25 June 1977), pp. 1440–1443. URL: https://link.aps.org/doi/10.1103/PhysRevLett.38.1440.

[15] Steven Weinberg. „A New Light Boson?" In: *Phys. Rev. Lett.* 40 (4 Jan. 1978), pp. 223–226. URL: https://link.aps.org/doi/10.1103/PhysRevLett.40.223.

[16] F. Wilczek. „Problem of Strong P and T Invariance in the Presence of Instantons". In: *Phys. Rev. Lett.* 40 (5 Jan. 1978), pp. 279–282. URL: https://link.aps.org/doi/10.1103/PhysRevLett.40.279.

[17] Georg G. Raffelt. „Astrophysical Axion Bounds". In: *Axions: Theory, Cosmology, and Experimental Searches*. Ed. by Markus Kuster, Georg Raffelt, and Berta Beltrán. Berlin, Heidelberg: Springer Berlin Heidelberg, 2008, pp. 51–71. URL: https://doi.org/10.1007/978-3-540-73518-2_3.

[18] Ciaran O'Hare. „Cosmology of axion dark matter". In: *Proceedings of 1st General Meeting and 1st Training School of the COST Action COSMIC WSIPers*. Sissa Medialab, Apr. 2024, p. 040. URL: http://dx.doi.org/10.22323/1.454.0040.

[19] Manuel Meyer, James Davies, and Julian Kuhlmann. „gammaALPs: An open-source python package for computing photon-axion-like-particle oscillations in astrophysical environments". In: *Proceedings of 37th International Cosmic Ray Conference — PoS*. ICRC2021. Sissa Medialab, June 2021, p. 557. URL: http://dx.doi.org/10.22323/1.395.0557.

[20] Tess R. Jaffe. „Practical Modeling of Large-Scale Galactic Magnetic Fields: Status and Prospects". In: *Galaxies* 7.2 (Apr. 2019), p. 52. URL: http://dx.doi.org/10.3390/galaxies7020052.

[21] M. S. Pshirkov et al. „DERIVING THE GLOBAL STRUCTURE OF THE GALACTIC MAGNETIC FIELD FROM FARADAY ROTATION MEASURES OF EXTRAGALACTIC SOURCES". In: *The Astrophysical Journal* 738.2 (Aug. 2011), p. 192. URL: http://dx.doi.org/10.1088/0004-637X/738/2/192.

[22] Beck, R. et al. „Systematic bias in interstellar magnetic field estimates". In: *A & A* 411.2 (Nov. 2003), pp. 99–107. URL: https://doi.org/10.1051/0004-6361:20031101.

[23] D. J. Watts et al. „COSMOGLOBE DR1 results: III. First full-sky model of polarized synchrotron emission from all WMAP and Planck LFI data". In: *Astronomy & Astrophysics* 686 (June 2024), A297. URL: http://dx.doi.org/10.1051/0004-6361/202348330.

[24] J. M. Cordes and T. J. W. Lazio. *NE2001.I. A New Model for the Galactic Distribution of Free Electrons and its Fluctuations*. 2003. arXiv: astro-ph/0207156 [astro-ph]. URL: https://arxiv.org/abs/astro-ph/0207156.

[25] J. M. Yao, R. N. Manchester, and N. Wang. „A NEW ELECTRON-DENSITY MODEL FOR ESTIMATION OF PULSAR AND FRB DISTANCES". In: *The Astrophysical Journal* 835.1 (Jan. 2017), p. 29. URL: https://dx.doi.org/10.3847/1538-4357/835/1/29.

[26] Carmelo Evoli et al. „Cosmic ray nuclei, antiprotons and gamma rays in the galaxy: a new diffusion model". In: *Journal of Cosmology and Astroparticle Physics* 2008.10 (Oct. 2008), p. 018. URL: https://dx.doi.org/10.1088/1475-7516/2008/10/018.

[27] Ronnie Jansson and Glennys R. Farrar. „A NEW MODEL OF THE GALACTIC MAGNETIC FIELD". In: *The Astrophysical Journal* 757.1 (Aug. 2012), p. 14. URL: http://dx.doi.org/10.1088/0004-637X/757/1/14.

[28] Manuel Meyer, James Davies, and Julian Kuhlmann. *gammALPs*. Version 0.4.1. Dec. 2023. URL: https://doi.org/10.5281/zenodo.10257944.

[29] Charles R. Harris et al. „Array programming with NumPy". In: *Nature* 585.7825 (Sept. 2020), pp. 357–362. URL: https://doi.org/10.1038/s41586-020-2649-2.

[30] Pauli Virtanen et al. „SciPy 1.0: Fundamental Algorithms for Scientific Computing in Python". In: *Nature Methods* 17 (2020), pp. 261–272. URL: https://doi.org/10.1038/s41592-019-0686-2.

[31] The Astropy Collaboration et al. „Astropy: A community Python package for astronomy". In: *A & A* 558 (2013), A33. URL: https://doi.org/10.1051/0004-6361/201322068.

[32] A. M. Price-Whelan et al. „The Astropy Project: Building an Open-science Project and Status of the v2.0 Core Package*". In: *The Astronomical Journal* 156.3 (Aug. 2018), p. 123. URL: http://dx.doi.org/10.3847/1538-3881/aabc4f.

[33] The Astropy Collaboration et al. „The Astropy Project: Sustaining and Growing a Community-oriented Open-source Project and the Latest Major Release (v5.0) of the Core Package*". In: *The Astrophysical Journal* 935.2 (Aug. 2022), p. 167. URL: http://dx.doi.org/10.3847/1538-4357/ac7c74.

[34] Siu Kwan Lam, Antoine Pitrou, and Stanley Seibert. „Numba: A llvm-based python jit compiler". In: *Proceedings of the Second Workshop on the LLVM Compiler Infrastructure in HPC*. 2015, pp. 1–6.

[35] R. Adam et al. „Planckintermediate results: XLII. Large-scale Galactic magnetic fields". In: *Astronomy & Astrophysics* 596 (Dec. 2016), A103. URL: http://dx.doi.org/10.1051/0004-6361/201528033.

[36] Michael Unger and Glennys Farrar. *The Coherent Magnetic Field of the Milky Way*. Version v1.0. Feb. 2024. URL: https://doi.org/10.5281/zenodo.10627091.

[37] Andrea Zonca et al. „healpy: equal area pixelization and spherical harmonics transforms for data on the sphere in Python". In: *Journal of Open Source Software* 4.35 (Mar. 2019), p. 1298. URL: https://doi.org/10.21105/joss.01298.

[38] M. Ajello et al. „Search for Spectral Irregularities due to Photon–Axionlike-Particle Oscillations with the Fermi Large Area Telescope". In: *Physical Review Letters* 116.16 (Apr. 2016). URL: http://dx.doi.org/10.1103/PhysRevLett.116.161101.

[39] Giorgio Galanti et al. „Observability of the Very-High-Energy Emission from GRB 221009A". In: *Physical Review Letters* 131.25 (Dec. 2023). URL: http://dx.doi.org/10.1103/PhysRevLett.131.251001.

[40] V. Lipunov et al. „GCN CIRCULAR n. 32634". In: (2022). URL: https://gcn.gsfc.nasa.gov/gcn3/32634.gcn3.

Eidesstattliche Erklärung

Ich versichere, dass ich die beigefügte schriftliche Bachelorarbeit selbstständig angefertigt und keine anderen als die angegebenen Hilfsmittel benutzt habe. Alle Stellen, die dem Wortlaut oder dem Sinn nach anderen Werken entnommen sind, habe ich in jedem einzelnen Fall unter genauer Angabe der Quelle deutlich als Entlehnung kenntlich gemacht. Dies gilt auch für alle Informationen, die dem Internet oder anderer elektronischer Datensammlungen entnommen wurden. Ich erkläre ferner, dass die von mir angefertigte Bachelorarbeit in gleicher oder ähnlicher Fassung noch nicht Bestandteil einer Studien- oder Prüfungsleistung im Rahmen meines Studiums war.

Ich bin damit einverstanden, dass die Bachelorarbeit veröffentlicht wird.

Hamburg, 03.09.2024

Ort, Datum

F. Landgraf

Unterschrift